Characterization of Mott-insulating and superfluid phases in the one-dimensional Bose–Hubbard model

Satoshi Ejima and Holger Fehske
Institut für Physik, Ernst-Moritz–Arndt Universität Greifswald, D-17489 Greifswald, Germany

Florian Gebhard and Kevin zu Münster
Fachbereich Physik, Philipps Universität Marburg, D-35032 Marburg, Germany

Michael Knap, Enrico Arrigoni, and Wolfgang von der Linden
Institute of Theoretical and Computational Physics, Graz University of Technology, A-8010 Graz, Austria

We use strong-coupling perturbation theory, the variational cluster approach (VCA), and the dynamical density-matrix renormalization group (DDMRG) method to investigate static and dynamical properties of the one-dimensional Bose–Hubbard model in both the Mott-insulating and superfluid phases. From the von Neumann entanglement entropy we determine the central charge and the transition points for the first two Mott lobes. Our DMRG results for the ground-state energy, momentum distribution function, boson correlation function decay, Mott gap, and single particle-spectral function are reproduced very well by the strong-coupling expansion to fifth order, and by VCA with clusters up to 12 sites as long as the ratio between the hopping amplitude and on-site repulsion, t/U, is smaller than 0.15 and 0.25, respectively. In addition, in the superfluid phase VCA captures well the ground-state energy and the sound velocity of the linear phonon modes. This comparison provides an authoritative estimate for the range of applicability of these methods. In strong-coupling theory for the Mott phase, the dynamical structure factor is obtained from the solution of an effective single-particle problem with an attractive potential. The resulting resonances show up as double-peak structure close to the Brillouin zone boundary. These high-energy features also appear in the superfluid phase which is characterized by a pronounced phonon mode at small momenta and energies, as predicted by Bogoliubov and field theory. In one dimension, there are no traces of an amplitude mode in the dynamical single-particle and two-particle correlation functions.

PACS numbers: 67.85.Bc, 67.85.De, 64.70.Tg

I. INTRODUCTION

The ability to place ultracold bosonic atoms in optical lattices offered new prospects in the study of quantum many-particle systems [1, 2], mainly because, in contrast to solid-state realizations, the properties of the system can be manipulated in a very controlled way by tuning the particle density, the lattice depth, the trapping potential and the interactions between the particles [3, 4]. Likewise, the spatial dimension and coordination number of the optical lattice, the degree of disorder, or the coupling strength to external fields might be changed [5, 6]. Hence, in these experiments, specific lattice Hamiltonians can be engineered and analyzed, including quantum phase transitions between gapped and itinerant phases. A prominent example is the transition between Mott insulating (MI) and superfluid (SF) phases which results from the competition between the particles' kinetic energy and their mutual on-site repulsion. In this way, subtle quantum correlation effects become observable on a macroscopic scale.

The Bose–Hubbard Hamiltonian captures the essential physics of interacting bosons in optical lattices [7]. The ground-state phase diagram of this model in two and three dimensions has been determined by analytical, perturbative methods [8–10] and numerical, quantum Monte-Carlo techniques [11–15]. The one-dimensional (1D) case, which can be realized experimentally [16], is also accessible by QMC [17], and particularly rewarding to study because the physics in 1D normally is rather peculiar [18].

On a linear chain with L sites and periodic boundary conditions (PBC) the Bose–Hubbard Hamiltonian reads

$$\begin{aligned} \hat{H} &= t\hat{T} + U\hat{D} \,, \\ \hat{T} &= -\sum_{j=1}^{L} (\hat{b}_j^\dagger \hat{b}_{j+1} + \hat{b}_{j+1}^\dagger \hat{b}_j) \,, \\ \hat{D} &= \frac{1}{2}\sum_{j=1}^{L} \hat{n}_j(\hat{n}_j - 1) \,. \end{aligned} \tag{1}$$

Here, $\hat{b}_j^\dagger$, $\hat{b}_j$, and $\hat{n}_j = \hat{b}_j^\dagger \hat{b}_j$ are the boson creation, annihilation and particle number operators on site j.

The grand-canonical Hamiltonian is given by $\hat{K} = \hat{H} - \mu\hat{N}$ where μ is the thermodynamic chemical potential and $\hat{N} = \sum_j \hat{n}_j$ counts the total number of particles. For N particles (atoms) in the system, the (global) filling factor is $\rho = N/L$.

In Eq. (1), the hopping of the bosons between neighboring sites is characterized by the tunneling amplitude t, while U is the on-site interaction which we choose to be repulsive, $U > 0$; recently, Nägerl et al. investigated an

unstable crystal of bosons with $U < 0$ [19]. Accordingly, the physics of the Bose–Hubbard model is governed by the ratio between kinetic energy and interaction energy, $x = t/U$. If, for given chemical potential μ, x is larger than a critical value the bosons are "superfluid". Below x_c, the system becomes Mott insulating, characterized by an integer filling factor ρ. In experiments, x can be varied over several orders of magnitude, by modifying the depth of the lattice through quantum optical techniques whereby SF and MI phases can be realized. From a theoretical point of view, the calculation of the boundaries between the SF and MI phases in the (μ, U) ground-state phase diagram is particularly demanding because quantum phase transitions in one dimension often are of Kosterlitz–Thouless type [18] with exponentially small Mott gaps in the vicinity of the transition.

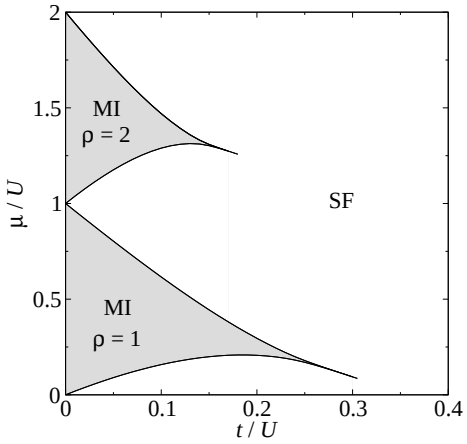

FIG. 1. Phase diagram of the 1D Bose–Hubbard model showing superfluid (SF) and Mott insulating (MI) regions as a function of the chemical potential μ/U and the electron transfer amplitude t/U. The boundaries delimiting the first two Mott lobes were determined by DMRG, using system sizes up to $L = 128$ and OBC [20], see text.

The numerical density-matrix renormalization group (DMRG) method [21, 22] is well suited to address one-dimensional interacting particle systems [3, 23, 24]. In fact, the (μ, U) ground-state phase diagram of the 1D Bose–Hubbard model has been obtained fairly accurately using this technique [20], see Fig. 1. Since multiple occupancies pose serious technical problems, the maximal boson number per site in DMRG is constrained to be five. Note that DMRG naturally works at fixed $N, L < \infty$, i.e., in the canonical ensemble. This leads to the definition of two chemical potentials for finite systems, $\pm\mu^{\pm}(L) = E_0(L, N \pm 1) - E_0(L, N)$ [24] where $E_0(L, N)$ denotes the ground-state energy. In the MI state we have a finite gap, $\Delta = \mu^+(L \to \infty) - \mu^-(L \to \infty) > 0$, whereas the chemical potential is continuous in the SF phase, $\mu = \mu^+(L \to \infty) = \mu^-(L \to \infty)$.

In one dimension, the delocalized SF state is not macroscopically occupied but rather characterized by an algebraic divergence of the momentum distribution [18, 25]. The localized MI state is incompressible, as usual, and characterized by an integer particle density and a gap in the single-particle spectrum [8]. The regions in the (μ, U) phase diagram where the density ρ is pinned to integer values are termed Mott lobes. Their special shape is conditioned by the strong phase fluctuations existing in a 1D system. Close to the boundaries of the Mott lobes, the Mott gap is exponentially small. The precise position of the Mott dips can be obtained from the Tomonaga–Luttinger parameter [20, 24].

A detailed theoretical understanding of the Bose–Hubbard model requires the calculations of (dynamical) correlation functions which poses a hard problem for which no exact solution exists. Recall that the 1D Bose–Hubbard model at $U < \infty$ (soft-core bosons) is not integrable. Consequently, a large variety of approximative approaches were suggested and elaborated for the Bose–Hubbard model and its variants during the last two decades; for a recent review see Ref. [26].

In the SF phase, (weakly) interacting bosons at low energies are well described as a Tomonaga–Luttinger liquid [8, 27]. However, close to the SF to MI transition, the precise character of the spectrum is still under debate. This particularly concerns the question whether or not a second, gapped mode besides the standard sound mode, as obtained from mean-field theory [28], can be seen in the single-particle spectral function or in the dynamical structure factor.

In the MI phase, strong-coupling expansions in $x = t/U$ give reliable analytical results. The ground-state energy of all Mott lobes was determined to second order by Freericks and Monien [29], and was improved up to order x^{14} for the lowest Mott lobe, $\rho = 1$, by Damski and Zakrzewski [30]. They also provided the series expansion for the local particle-density fluctuations to order x^{13}, a high-order series expansion for the single-particle density matrix $P(r) = \mathcal{O}(x^r)$ for $r = 1, 2, 3$, and gave the corresponding expressions for the ground-state density-density correlation function $D(r) - 1 = \mathcal{O}(x^{2r})$ for $r = 1, 2, 3$; for results for $r \leq 6$ and $r \leq 10$, respectively, see Ref. [9]. The Fourier transformation of $P(r)$ provides the momentum distribution $n(k)$. The result for $n(k)$ to third order in x was re-derived by Freericks et al. [10] using a different method.

In contrast to higher dimensions, $d \geq 2$, the convergence of the strong-coupling expansion series in 1D is rather questionable. These problems become apparent, e.g., in the calculation of the critical value x_c for the transition between the Mott insulator and the superfluid phase. For example, the series expansion for the superfluid susceptibility constructed by Eckardt et al. [9] determines x_c very accurately in $d \geq 2$ but fails for $d = 1$ where a reentrant superfluid phase is predicted [9, 23].

High-order expansions are also possible for the single-particle gap [31]. The Mott transition in one dimension is of Kosterlitz–Thouless (KT) type so that the gap becomes exponentially small close to the transition, which

cannot be reproduced easily within a third-order strong-coupling expansion [29]. In order to obtain a good approximation of the critical value for the transition, Elstner and Monien [32] proposed a scaling analysis for the gap. Based on this idea, Freericks et al. [10] used a (6,7)–Padé approximant for the square of the logarithm of the single-particle gap to find $x_c \approx 0.300(1)$ for $\rho = 1$, in good agreement with the DMRG value; for another scheme, see Heil and von der Linden [33].

In the present paper, we first refine and extend the perturbative strong-coupling approach in order to analyze the single-particle spectral function and the dynamical structure factor. For the latter quantity, we obtain higher-order corrections from the corresponding Green's function. Secondly, in order to relax the strong-coupling condition, we employ the variational cluster approach (VCA) that is applicable in both the Mott insulating and the superfluid phase [34–37]. For the calculation of spectral properties in the SF phase, the VCA can be reformulated in terms of a pseudo-particle approach, whereby single-particle excitations within a cluster are approximately mapped onto particle-like excitations [36], or in terms of the self-energy functional approach [37, 38]. Thirdly, we perform large-scale DMRG calculations: (i) to access the whole parameter space of the Bose–Hubbard model and (ii) to benchmark the reliability of the used analytical strong-coupling and numerical VCA techniques. While in the past DMRG has been successfully applied to investigate the ground-state properties of the Bose–Hubbard model [3, 23, 24], DMRG results for dynamical properties at zero temperatures are rare (in contrast to fermionic systems), but highly desirable because superfluids in optical lattices can be studied by momentum-resolved Bragg spectroscopy [39–42].

The outline of this paper is as follows. In Sect. II we describe perturbative approaches to the Bose–Hubbard model, and present a detailed derivation of the strong-coupling results for static and dynamical quantities. Sects. III and IV sketch the specifics of the VCA and DMRG, respectively, when applied to the Bose–Hubbard model. Sect. V contains our main results. In particular, we discuss how the von Neumann entanglement entropy can be calculated from DMRG and how it can be used to determine the KT transition point in the Mott lobes. Next, we determine the ground-state energy, the boson correlation function, and the momentum distribution function. Lastly, we analyze the photoemission spectra and dynamical structure factors. In all cases, we compare analytical and numerical results. Finally, Sect. VI summarizes our findings.

II. PERTURBATIVE APPROACHES

A. Weak-coupling limit

For weak interactions, we use the perturbative results obtained by Bogoliubov [43] (see Fetter and Walecka, chap. 35 [44]), for a weakly interacting Bose gas with contact interaction and density $\rho = N/L$. From the textbook formulae we find for the 1D Bose–Hubbard Hamiltonian at $\rho = 1$

$$\epsilon(k) = -2t(\cos(k) - 1)\,, \tag{2}$$

$$E(k) = \sqrt{\epsilon(k)(\epsilon(k) + 2U)}\,, \tag{3}$$

$$\frac{N_0}{L} = 1 - \frac{1}{2L}\sum_{k\neq 0}\left(\frac{\epsilon(k)+U}{E(k)} - 1\right)\,, \tag{4}$$

where $\epsilon(k)$ is the bare dispersion of (1) shifted by $2t$, $E(k)$ is the dispersion of the Bogoliubov quasiparticles, and N_0 is the number of particles in the condensate. Here, $k = 2\pi m_k/L, m_k = 0, 1, \ldots, L-1$ are the crystal momenta for PBC. The Bogoliubov ground-state energy reads

$$\frac{E_0^{\mathrm{B}}(U)}{L} = -2t + \frac{U}{2} + \frac{1}{2L}\sum_{k\neq 0}\left(E(k) - \epsilon(k) - U\right)\,. \tag{5}$$

Two problems with the Bogoliubov theory become apparent when we consider some limits. First, we address the limit $k \to 0$ for $E(k)$, $E(k \to 0) \sim k$. Therefore, in the thermodynamic limit, the integral in Eq. (4) is logarithmically divergent, and $N_0 = 0$ in 1D results, in agreement with field theory [18]. This, however, invalidates the starting point of the Bogoliubov approximation. Second, we cannot apply the theory for large U/t because $E(k, U \gg t) \approx \sqrt{8Ut}|\sin(k/2)|$ so that $(E_0^{\mathrm{B}}(U \gg t)/L) \sim \sqrt{Ut}$ for large U/t, in contrast with the exact limit, $\lim_{U\to\infty} E_0(U) = 0$.

The analytical result for the ground-state energy in Bogoliubov theory is found, e.g. using MATHEMATICA [45], as

$$\frac{E_0^{\mathrm{B}}(U)}{L} = -3t + \frac{\sqrt{2Ut}}{\pi} + \frac{U+2t}{\pi}\arccos\left(\sqrt{\frac{U}{U+2t}}\right)\,. \tag{6}$$

The small-U expansion is

$$\frac{E_0^{\mathrm{B}}(U \ll t)}{Lt} = -2 + \frac{U}{2t} - \frac{\sqrt{2}(U/t)^{3/2}}{3\pi}\,. \tag{7}$$

Corrections are of the order $(U/t)^{5/2}$ which is formally beyond the validity of the Bogoliubov expansion which ignores terms of the order $(U/t)^2$.

B. Strong-coupling limit

1. Harris–Lange transformation

For the bosonic Hubbard model, an $x = t/U$ strong-coupling expansion easily permits the calculation of the ground state for $x \to 0$,

$$|\phi_0\rangle = \frac{1}{(\rho!)^{L/2}}\prod_i \left(\hat{b}_i^\dagger\right)^\rho |\mathrm{vac}\rangle\,, \tag{8}$$

because it is non-degenerate for the Mott lobe with integer filling $\rho = N/L$. Likewise, the energy levels of a single-hole excitation, $E_{\rm h}(k)$, and of a single-particle excitation, $E_{\rm p}(k)$, can be determined to high order in x because the perturbation theory for these energy levels also starts from non-degenerate states, e.g., for $\rho = 1$,

$$|\phi_{\rm h}(k)\rangle = \sqrt{\frac{1}{L}} \sum_{l=1}^{L} e^{-{\rm i}kl} \hat{b}_l |\phi_0\rangle \; , \tag{9}$$

$$|\phi_{\rm p}(k)\rangle = \sqrt{\frac{1}{L}} \sqrt{\frac{1}{2!}} \sum_{l=1}^{L} e^{{\rm i}kl} \hat{b}_l^\dagger |\phi_0\rangle \; . \tag{10}$$

When we employ the unitary Harris–Lange transformation [46], the strong-coupling Hamiltonian of the Bose–Hubbard model can be derived in a systematic way,

$$\hat{h} = e^{\hat{S}} \hat{H} e^{-\hat{S}} = U\hat{D} + t \sum_{r=0}^{\infty} x^r \hat{h}_r \; , \tag{11}$$

$$\hat{S} = -\hat{S}^\dagger = \sum_{r=1}^{\infty} x^r \hat{S}_r \; . \tag{12}$$

In practice, a finite order in the expansion of $\hat{S}$ is kept. When we retain $\hat{S}_r$ for $1 \le r \le n$, we denote this the 'nth-order approximation'. In nth order we thus keep $(n-1)$ terms in the expansion for $\hat{h}$ whose terms obey $[\hat{h}_r, \hat{D}]_- = 0$ for $0 \le r \le n-1$. To order $(n-1)$, the number of double occupancies is conserved by $\hat{h}$. This defines the construction principle for the operators $\hat{S}_n$.

The leading order terms for $\hat{S}_r$ and $\hat{h}_r$ are given by

$$\hat{S}_1 = \sum_{D_1, D_2} \frac{\hat{P}_{D_1} \hat{T} \hat{P}_{D_2}}{D_1 - D_2} \; , \tag{13}$$

$$\hat{S}_2 = \sum_{D_1, D_2} \frac{-\hat{P}_{D_1} \hat{T} \hat{P}_{D_1} \hat{T} \hat{P}_{D_2} + \hat{P}_{D_1} \hat{T} \hat{P}_{D_2} \hat{T} \hat{P}_{D_2}}{(D_1 - D_2)^2} + \sum_{D_1, D_2, D_3} \frac{\hat{P}_{D_1} \hat{T} \hat{P}_{D_3} \hat{T} \hat{P}_{D_2}}{2(D_1 - D_2)} \frac{[D_1 - D_3 + D_2 - D_3]}{(D_1 - D_3)(D_2 - D_3)} \; , \tag{14}$$

$$\hat{h}_0 = \sum_{D} \hat{P}_D \hat{T} \hat{P}_D \; , \tag{15}$$

$$\hat{h}_1 = \sum_{D_1, D_2} \frac{\hat{P}_{D_1} \hat{T} \hat{P}_{D_2} \hat{T} \hat{P}_{D_1}}{D_1 - D_2} \; , \tag{16}$$

where $\hat{P}_D$ is the projection operator onto the subspace of eigenstate with D interactions, $\hat{D} = \sum_{D=0}^{\infty} D \hat{P}_D$. In the above sums it is implicitly understood that all indices $D_i \ge 0$ are mutually different. A compact formula for the recursive generation of higher orders can be found in Ref. [47]. In our analysis, we use a computer program to generate orders $r \ge 2$ in $\hat{S}_r$ and $\hat{h}_r$ [48].

For the exact ground state of the Mott insulator we have

$$\hat{H}|\psi_0\rangle = E_0 |\psi_0\rangle \; , \tag{17}$$

where E_0 is the exact ground-state energy. Within the strong-coupling expansion we then find

$$|\psi_0\rangle = e^{\hat{S}} |\phi_0\rangle \quad ; \quad \hat{h}|\phi_0\rangle = E_0 |\phi_0\rangle \; , \tag{18}$$

where $|\phi_0\rangle$ is the ground state of $\hat{h}_{-1} = \hat{D}$, see Eq. (8).

Since the Harris–Lange transformation is unitary, operators and ground-state expectation values translate according to

$$\begin{aligned} |\psi_0\rangle &\mapsto |\phi_0\rangle \; , \\ \hat{H} &\mapsto \hat{h} \; , \\ \hat{A} &\mapsto \widetilde{A} = e^{\hat{S}} \hat{A} e^{-\hat{S}} \; . \end{aligned} \tag{19}$$

The series expansion for $\hat{S}$ to nth order contains n powers of the kinetic energy operator $\hat{T}$. Therefore, local operators $\hat{A}_i$ translate into cluster operators which involve the sites l with $|l - i| \le n$. The range of $\hat{h}$ scales accordingly: the strong-coupling theory generates a cluster expansion.

2. *Static quantities*

For fixed momentum k, the exact eigenstates of $\hat{h}$ with one extra particle or one hole in $|\phi_0\rangle$, Eq. (8), are given by the hole and particle states defined in Eqs. (9), (10). In this sector, we thus obtain the ground-state energy and the single-particle excitation energies from

$$E_0 = \langle \phi_0 | \hat{h} | \phi_0 \rangle \; , \tag{20}$$

$$E_{\rm p}(k) = \langle \phi_{\rm p}(k) | \hat{h} | \phi_{\rm p}(k) \rangle - E_0 \; , \tag{21}$$

$$E_{\rm h}(k) = \langle \phi_{\rm h}(k) | \hat{h} | \phi_{\rm h}(k) \rangle - E_0 \; . \tag{22}$$

Up to and including 6th order in x, we obtain for the ground-state energy per site

$$\frac{E_0^{[6]}}{4UL} = -x^2 + x^4 + \frac{68}{9} x^6 + \mathcal{O}(x^8) \; , \tag{23}$$

in agreement with Ref. [30].

The single-hole and single-particle excitations energies are

$$\begin{aligned} \frac{E_{\rm h}(k)}{t} = {} & 8x - \frac{512}{3} x^5 \\ & + \left(-2 + 12x^2 - \frac{224}{3} x^4 \right) \cos(k) \\ & + \left(-4x + 64x^3 - \frac{1436}{3} x^5 \right) \cos(2k) \\ & + \left(-12x^2 + 276x^4 \right) \cos(3k) \\ & + \left(-44x^3 + 1296x^5 \right) \cos(4k) \\ & - 180x^4 \cos(5k) - 792x^5 \cos(6k) + \mathcal{O}\left(x^6\right) \; , \end{aligned} \tag{24}$$

and

$$\frac{E_{\rm p}(k)}{t} = \frac{1}{x} + 5x - \frac{513}{20}x^3 - \frac{80139}{200}x^5 + \left(-4 + 18x^2 - \frac{137}{150}x^4\right)\cos(k) + \left(-4x + 64x^3 - \frac{426161}{1500}x^5\right)\cos(2k) + \left(-12x^2 + 276x^4\right)\cos(3k) + \left(-44x^3 + 1296x^5\right)\cos(4k) - 180x^4\cos(5k) - 792x^5\cos(6k) + \mathcal{O}\left(x^6\right) . \quad (25)$$

The single-particle gap is calculated from $\Delta = E_{\rm p}(0) + E_{\rm h}(0)$ which results in

$$\frac{\Delta}{U} = 1 - 6x + 5x^2 + 6x^3 + \frac{287}{20}x^4 + \frac{5821}{50}x^5 - \frac{602243}{1000}x^6 + \dots , \quad (26)$$

in agreement with Ref. [31].

3. Single-particle spectral functions

The single-particle spectral functions are obtained from

$$A^+(k,\omega) = \sum_n \left|\langle\phi_n|\hat{b}^\dagger(k)|\phi_0\rangle\right|^2 \delta\left(\omega - \omega_n^+\right) , \quad (27)$$

$$A^-(k,\omega) = \sum_n \left|\langle\phi_n|\hat{b}(k)|\phi_0\rangle\right|^2 \delta\left(\omega + \omega_n^-\right) , \quad (28)$$

where $\omega_n^\pm = E_n - E_0$ is the excitation energy of the exact eigenstates $|\phi_n\rangle$ of $\hat{h}$ with $N = \rho L \pm 1$ bosons, measured from the ground-state energy, and

$$\hat{b}(k) = \sqrt{\frac{1}{L}}\sum_{l=1}^{L} e^{-{\rm i}kl}\hat{b}_l , \; \hat{b}^\dagger(k) = \sqrt{\frac{1}{L}}\sum_{l=1}^{L} e^{{\rm i}kl}\hat{b}_l^\dagger \quad (29)$$

for PBC. Obviously, the single-particle gap Δ is obtained from $\Delta = {\rm Min}_n(\omega_n^+) - {\rm Max}_n(-\omega_n^-)$.

For the calculation of the spectral function, we need the weight factors

$$w_{\rm p}(k) = \left|\langle\phi_{\rm p}(k)|k_+\rangle\right|^2 , \; |k_+\rangle = \widetilde{b}_k^\dagger|\phi_0\rangle , \quad (30)$$

$$w_{\rm h}(k) = \left|\langle\phi_{\rm h}(k)|k_-\rangle\right|^2 , \; |k_-\rangle = \widetilde{b}_k|\phi_0\rangle . \quad (31)$$

Up to and including third order in x we find

$$w_{\rm h}(k) = \Big[1 - 4x^2 + \left(4x - 20x^3\right)\cos(k) + 14x^2\cos(2k) + 60x^3\cos(3k)\Big]^2 , \quad (32)$$

$$w_{\rm p}(k) = 2\Big[1 - \frac{7}{4}x^2 + \left(2x - \frac{15}{4}x^3\right)\cos(k) + 8x^2\cos(2k) + 18x^3\cos(3k)\Big]^2 . \quad (33)$$

The weights $w_{\rm p,h}(k)$ are those of the lower and upper Hubbard bands which are energetically closest to the single-particle gap and separated by U in the atomic limit.

In higher orders of the strong-coupling expansion, secondary Hubbard bands appear in the single-particle spectral function [35, 46, 49, 50]. This can most easily be seen from the weights which express the overlap of the exact excited eigenstates of $\hat{h}$ with the states $|k_\pm\rangle$ see Eqs. (30), (31). With an amplitude of the order x^2, the state $|k_-\rangle$ contains a component with two neighboring holes and one doubly occupied site in a row. This component is *not* in the original subspace with $D = 0$ and contributes to the upper Hubbard band with weight x^4. Therefore, for the weight of the lower Hubbard band we have

$$w_{\rm LHB}(k) = w_{\rm h}(k) + \mathcal{O}(x^4) = 1 + (8x - 16x^3)\cos(k) + 36x^2\cos(2k) + 176x^3\cos(3k) + \mathcal{O}(x^4) . \quad (34)$$

The state $|k_+\rangle$ contains configurations with a triple occupancy and a neighboring hole to the left or right. Their amplitude up to order x^2 is $a_\pm(k) = \sqrt{6}(x/2 - \exp(\pm{\rm i}k)x^2/3)$. They contribute to the secondary Hubbard band centered around $\omega = 3U$ to order x^2 and x^3. Components with two double occupancies and a quadruple occupancies have an amplitude proportional to order x^2 and thus contribute to the bands centered around $\omega = 2U$ and $\omega = 6U$, respectively, with weights of the order of x^4. Up to and including order x^3, the secondary Hubbard band around $\omega = 3U$ has the weight

$$w_{3U}(k) = 12\left|\frac{x}{2} - \frac{x^2 e^{-{\rm i}k}}{3}\right|^2 + \mathcal{O}\left(x^4\right) . \quad (35)$$

Therefore, the total weight for the upper Hubbard bands is given by $w_{\rm UHB}(k) = w_{\rm p}(k) + w_{3U}(k) = 1 + w_{\rm LHB}(k)$, in agreement with the sum rule

$$\int_{-\infty}^{\infty} {\rm d}\omega[A^+(k,\omega) - A^-(k,\omega)] = w_{\rm UHB}(k) - w_{\rm LHB}(k) = 1 , \quad (36)$$

which follows directly from the definition of the spectral function. Another check results from the momentum distribution sum rule,

$$w_{\rm LHB}(k) = \int_{-\infty}^{\infty} {\rm d}\omega A^-(k,\omega) = \langle\phi_0|\hat{b}^\dagger(k)\hat{b}(k)|\phi_0\rangle = n(k) . \quad (37)$$

Up to and including third order in x, our results for $n(k)$ agree with those found in Refs. [10, 30].

4. Dynamical structure factor

For the density-density correlation function we focus on $\omega > 0$ so that we do not have to consider terms of the form $\langle\phi_0|\widetilde{n}_{l+r}\delta\left(\omega - (\hat{h} - E_0)\right)|\phi_0\rangle \sim \delta(\omega)$. We define the states

$$|q\rangle = \left(\widetilde{n}_q - \hat{n}_q\right)|\phi_0\rangle , \quad (38)$$

where the density operator in momentum space is given by ($q = 2\pi m_q/L, m_q = 0, 1, \ldots, L-1$)

$$\hat{n}(q) = \sum_{l=1}^{L} e^{\mathrm{i}ql}\hat{n}_l = \sum_k \hat{b}^\dagger(k+q)\hat{b}(k) = (\hat{n}(-q))^\dagger \ . \quad (39)$$

Then, we can express the dynamical structure factor in the form

$$\begin{aligned} S(q,\omega>0) &= \sum_{l=1}^{L} e^{-\mathrm{i}ql} S_l(\omega) = \langle q|\delta\left(\omega - (\hat{h}-E_0)\right)|q\rangle \\ &= \sum_n |\langle \Phi_n|q\rangle|^2\, \delta\left(\omega-(\hat{h}-E_0)\right) \ , \end{aligned} \quad (40)$$

where $|\Phi_n\rangle$ are the exact eigenstates of $\hat{h}$ in the sector with $N = \rho L$ bosons.

Leading order contribution. The dynamical structure factor was calculated analytically within mean-field theory [28], bosonization [26, 51], and lowest-order strong-coupling theory [51–53].

The strong-coupling result to leading order is readily obtained from the exact eigenstates of $\hat{h}_0$, Eq. (15), in the sector with one hole and one double occupancy. The subspace ($N = L, D = 1$) is spanned by the $L(L-1)$ orthonormal states ($l \neq L$)

$$|q,l\rangle = \sqrt{\frac{1}{L}}\sum_{s=1}^{L} e^{\mathrm{i}qs}|s,l\rangle \ , \ |s,l\rangle = \sqrt{\frac{1}{2}}\hat{b}_s^\dagger \hat{b}_{s+l}|\phi_0\rangle \ . \quad (41)$$

The states $|q,l\rangle$ obey the effective single-particle Schrödinger equation

$$\begin{aligned} \hat{h}_0|q,l\rangle = &-(1-\delta_{l,1})(1+2e^{-\mathrm{i}q})|q,l-1\rangle \\ &-(1-\delta_{l,L-1})(1+2e^{\mathrm{i}q})|q,l+1\rangle \ . \end{aligned} \quad (42)$$

As expected for a translational invariant system, the center-of-mass momentum $q = 2\pi m_q/L$ with $m_q = 0, 1, \ldots, L-1$ is conserved.

The leading-order contribution to the states $|q\rangle = \sum_{n=1}^{\infty} x^n |q^{[n]}\rangle$ from (38) is given by

$$|q^{[1]}\rangle = \sqrt{2}\left[(1-e^{\mathrm{i}q})|q,1\rangle + (1-e^{-\mathrm{i}q})|q,L-1\rangle\right] \ , \quad (43)$$

i.e., double occupancy and hole are nearest neighbors.

Eq. (42) describes a single particle on an open chain with $L-1$ sites which reflects the fact that hole and double occupancy cannot be on the same site, $l \neq L$. In contrast to the fermionic case, the hard-core constraint is not sufficient to determine the phase shift between hole and double occupancy because their tunnel amplitudes differ by a factor of two. Therefore, the scattering phase shift between double occupancy and hole is not trivial [51–53]. This is in contrast to the mean-field approach [28] where the bare dispersions for hole and double occupancy enter Eq. (40).

The normalized double-occupancy–hole eigenstates are given by

$$|q;k\rangle = \sqrt{\frac{2}{L}}\sum_{l=1}^{L-1} \sin(kl) e^{\mathrm{i}\phi(q)l}|q,l\rangle \quad (44)$$

with $k = (\pi/L)m_k$ ($m_k = 1, 2, \ldots, L-1$) where the two-particle phase shift $\phi(q)$ follows from

$$\tan[\phi(q)] = \frac{2\sin(q)}{1+2\cos(q)} \ . \quad (45)$$

The energies of the eigenstates $|q;k\rangle$ of $t\hat{h}_0$ are given by

$$E(q,k) = -2t\cos(k)\sqrt{5+4\cos(q)} \ . \quad (46)$$

The overlap with the states in Eq. (43) defines the oscillator strengths in Eq. (38),

$$\begin{aligned} \langle q;k|q^{[1]}\rangle = \sqrt{2}\sqrt{\frac{2}{L}}\sin(k)\Big[&(1-e^{\mathrm{i}q})e^{-\mathrm{i}\phi(q)} \\ &-(1-e^{-\mathrm{i}q})(-1)^{m_k}e^{-\mathrm{i}\phi(q)(L-1)}\Big] \ , \end{aligned} \quad (47)$$

so that, in the thermodynamic limit ($L \to \infty$), we obtain for the weights

$$w(q;k) = \left(\frac{t}{U}\right)^2 \frac{32}{L}\sin^2(k)\sin^2(q/2) \ , \quad (48)$$

where we dropped the cross terms because their contribution to the structure factor vanishes due to the fast oscillations of $(-1)^{m_k}$.

The dynamical structure factor becomes for $\omega > 0$

$$\begin{aligned} S^{[1]}(q,\omega) = 2&\left(\frac{4t\sin(q/2)}{U}\right)^2 \\ &\times \int_0^\pi \frac{\mathrm{d}k}{\pi}\sin^2(k)\delta\left(\omega - U - E(q,k)\right) \ . \end{aligned} \quad (49)$$

Finally, for $|\omega - U| \leq 2t\sqrt{5+4\cos(q)}$ we obtain ($t \equiv 1$)

$$S^{[1]}(q,\omega) = \left(\frac{4\sin(q/2)}{U}\right)^2 \frac{\sqrt{20+16\cos(q)-(\omega-U)^2}}{2\pi(5+4\cos(q))} \quad (50)$$

for the dynamical structure factor to leading order [51–53].

Second-order and higher-order contributions. For the next order in the (t/U)-expansion we must calculate the action of $\overline{h}_1 \equiv \hat{h}_1 - E_0^{[1]}$ on the states $|q,l\rangle$, where we use $E_0 = t\sum_{n=1}^{\infty} x^n E_0^{[n]}$. The correction to Eq. (42) reads

$$\begin{aligned} \overline{h}_1|q,l\rangle = &13|q,l\rangle \\ &-2\left[(1-\delta_{l,1})(1-\delta_{l,2})(1+e^{-2\mathrm{i}q})|q,l-2\rangle\right] \\ &-2\left[(1-\delta_{l,L-1})(1-\delta_{l,L-2})(1+e^{2\mathrm{i}q})|q,l+2\rangle\right] \\ &+2\delta_{l,1}\Big[(-\frac{1}{4}+e^{-\mathrm{i}q}+e^{\mathrm{i}q})|q,1\rangle \\ &\qquad +(\frac{1}{4}+e^{-\mathrm{i}q}+e^{-2\mathrm{i}q})|q,L-1\rangle\Big] \\ &+2\delta_{l,L-1}\Big[(\frac{1}{4}+e^{\mathrm{i}q}+e^{2\mathrm{i}q})|q,1\rangle \\ &\qquad +(-\frac{1}{4}+e^{-\mathrm{i}q}+e^{\mathrm{i}q})|q,L-1\rangle\Big] \ . \end{aligned} \quad (51)$$

The effective single-particle problem contains an overall energy shift $13t^2/U$, a nearest-neighbor transfer $l \to (l+1)$ with amplitude $t(q) = (-t)(1+2\cos(q)+2\mathrm{i}\sin(q))$ as before, an additional next-nearest neighbor transfer from $l \to l+2$ with amplitude $m(q) = -2(t^2/U)(1+\cos(2q)+\mathrm{i}\sin(2q))$, and a potential at the chain ends, $V_{1,1} = V_{L-1,L-1} = (t^2/U)(4\cos(q) - 1/2)$ and $V_{1,L-1} = V^*_{L-1,1} = (2t^2/U)(1/4 + \cos(q) + \cos(2q) + \mathrm{i}\sin(q) + \mathrm{i}\sin(2q))$.

Now that the potential links the two chain ends, it is computational advantageous to treat the problem on a ring instead of a chain. The potential is readily generalized according to Eq. (51). For a ring, the potential also contains the terms $V_{1,L-2}$ and $V_{2,L-1}$ and their complex conjugates so that the potential links four neighboring sites. Moreover, the extension of $\hat{h}_0$ from a chain to a ring generates corrections to $V_{1,L-1}$ and $V_{L-1,1}$.

The x^2-corrections to the states $|q\rangle$ (38) read

$$|q^{[2]}\rangle = 3\sqrt{2}\left[(1-e^{2\mathrm{i}q})|q,2\rangle + (1-e^{-2\mathrm{i}q})|q,L-2\rangle\right] . \tag{52}$$

As the potential $V_{a,b}$, the dynamical structure factor to second order involves the four neighboring sites $l = L-2, L-1, 1, 2$.

The calculation of all eigenstates of $\hat{h}_0 + \hat{h}_1$ is not feasible in the thermodynamic limit. To calculate the dynamical structure factor we address the corresponding Green's function

$$G_{a,b}(q,z) = \langle q,a|\frac{1}{z-(\hat{h}-E_0)}|q,b\rangle . \tag{53}$$

For the structure factor in leading order, Eq. (43) requires the four Green's functions $G_{a,b}(q,\omega+\mathrm{i}0^+)$ for $a,b = 1, L-1$. The second order requires the Green's function for $a,b = 1,2,L-2,L-1$. This cluster principle generalizes to higher orders, i.e., in nth order we have to calculate a $(2n)\times(2n)$ matrix of Green's functions for a potential which links $2n$ neighboring sites.

The Green's function of a particle in a potential of finite range is readily calculated [54]. We start from $\hat{h} = \hat{t} + \hat{V}$, where $\hat{t}$ describes the free particle motion over the ring with dispersion relation $\varepsilon_q(k)$; up to second order, we have $\varepsilon_q^{(2)}(k) = -2t[\cos(k)+2\cos(k-q)] + 13(t^2/U) - 4(t^2/U)[\cos(2k)+\cos(2k-2q)]$ with $0 \le k < 2\pi$. In the thermodynamic limit, the free Green's function is readily calculated,

$$g_{a,b}(q,z) = \langle q,a|\frac{1}{z-\hat{t}}|q,b\rangle = \int_{-\pi}^{\pi}\frac{\mathrm{d}k}{2\pi}\frac{e^{\mathrm{i}k(a-b)}}{z-\varepsilon_q(k)} , \tag{54}$$

where we use the fact that the free states are plane waves. We calculate the free Green's functions for $z = \omega \pm \mathrm{i}0^+$ with the help of the residue theorem. Therefore, their real and imaginary parts are available with high accuracy for all real frequencies $\omega > 0$.

With the help of the operator identity

$$\frac{1}{z-\hat{t}-\hat{V}} = \frac{1}{z-\hat{t}} + \frac{1}{z-\hat{t}}\hat{V}\frac{1}{z-\hat{t}-\hat{V}} \tag{55}$$

we derive the Green's function (53) from the equation

$$G_{a,b}(q,z) = g_{a,b}(q,z) + \sum_{l,m} g_{a,l}(q,z)V_{l,m}G_{m,b}(q,z) . \tag{56}$$

This matrix equation has the formal solution

$$\underline{\underline{G}}(q,z) = \left(\underline{\underline{1}} - \underline{\underline{g}}(q,z)\underline{\underline{V}}\right)^{-1}\underline{\underline{g}}(q,z) . \tag{57}$$

In nth-order perturbation theory, the potential and the required Green's functions have the same range $2n$ on the lattice. Therefore, the matrix problem in (57) reduces to the inversion of a $2n\times 2n$-matrix for fixed $(q, z = \omega \pm \mathrm{i}0^+)$.

The Green's function calculation provides higher-order corrections to $S^{[1]}(q,\omega)$. In Sect. V we show results for the dynamical structure factor to fifth order in the (t/U)-expansion in the region around $\omega = U$.

The Green's function calculation does *not* cover the higher Hubbard sub-bands. The first contribution to the structure factor $S(q,\omega)$ beyond $\omega \approx U$ occurs around $\omega = 3U$ with intensity x^4. In the regions where strong-coupling perturbation theory is reliable, $x \lesssim 0.15$, the secondary bands contribute only a few percent of the total weight. When we include the term to order x^4 in the frequency-integrated structure factor, the sum-rule for the structure factor is fulfilled, i.e., we reproduce the terms $D(r)$ of the ground-state density-density correlation function for $r = 1,2,3$ [30] up to and including x^4.

III. VARIATIONAL CLUSTER APPROACH

The basic idea of the VCA is to approximate the self-energy Σ of a strongly correlated, physical system $\hat{H}$ by the self-energy of an exactly solvable reference system $\hat{H}'$ [55]. Both the physical and the reference system share the same interaction but differ in their single-particle terms. The optimal self-energy is determined self-consistently from a stationary condition on the grand-canonical potential Ω,

$$\frac{\delta\Omega}{\delta\Sigma} = 0 . \tag{58}$$

To evaluate this expression, the self-energy is parameterized by the single-particle parameters of the reference system. In fact, this idea is quite general and allows to unify (cluster)-Dynamical Mean Field Theory and VCA within the same theoretical framework depending on the choice of the reference system [38, 56]. In the case of the VCA, the reference system is chosen to be a cluster decomposition of the physical system with modified single-particle parameters. Furthermore, the reference system is selected such that it can be solved exactly. In principle, any many-body cluster solver at hand can be used which provides the dynamic single particle Green's function. Here, we use Lanczos exact diagonalization [35, 57].

Originally, VCA was introduced for fermionic systems [55]. For correlated lattice bosons, it first has

been in use to investigate the normal, Mott insulating phase [34]. In Refs. [36, 37] VCA has been extended to the superfluid phase. This extension adopts the Nambu notation and is applicable to a large class of lattice models that exhibit a condensed phase. Since VCA is in the end a form of a cluster mean-field approach, it can obviously not comprise fluctuations at length scales larger than the cluster size. This means that in the case of power-law decaying correlations as present here, these are spuriously replaced by long-range order in the VCA. This is a common issue of all mean-field like approaches. Despite this drawback, VCA still provides reliable results for many observables such as the ground-state energy, the sound velocity of the phonon excitations, and the single-particle spectral function.

Explicitly, the grand potential for bosonic systems with normal and the superfluid components is given by [36, 37]

$$\begin{aligned} 2\Omega = 2\Omega' - \mathrm{Tr}\ln(-G) + \mathrm{Tr}\ln(-G') - \mathrm{Tr}(\underline{\underline{t}} - \underline{\underline{t}}') \\ + \langle\hat{A}\rangle^\dagger [G_{(0)}]^{-1} \langle\hat{A}\rangle - \langle\hat{A}'\rangle^\dagger [G'_{(0)}]^{-1} \langle\hat{A}'\rangle \ , \end{aligned} \quad (59)$$

where G is the interacting Green's function, $\underline{\underline{t}}$ is the single-particle Hamiltonian matrix, $\langle\hat{A}\rangle$ denotes expectation values of the Nambu boson operators consisting of both creation and annihilation operators, and the subscript '(0)' indicates that the Green's function is evaluated at zero wavevector and zero frequency. In (59), the prime marks again reference system quantities. The first line of (59) is identical to the expression in the normal phase [34] apart from the fact that the Green's functions are considered to be in Nambu space and thus contain anomalous parts which also account for the factor 1/2. The second line takes care of the condensation of bosons, which in one dimension is an artifact of the dynamical and self-consistent mean-field treatment, as discussed above.

To obtain the results presented below, we always use the chemical potential of the reference system and a field which breaks the $U(1)$ symmetry on the level of the reference system as variational parameters. In the Mott phase we also determine the intercluster hopping and the boundary energies of the reference system self-consistently [50]. Having found the stationary point of the grand potential Ω with respect to the variational parameters, we evaluate the dynamical single particle Green's function $G(k,\omega)$ of the physical system [36, 37]. From that we calculate the single-particle spectral function $A(k,\omega) = -\mathrm{Im}\, G(k,\omega)/\pi$. The static density-density correlation functions can be obtained from the Fourier transform of the momentum distribution function, as specified in Ref. [50].

IV. DMRG APPROACH

The DMRG allows us to calculate static, dynamic and spectral properties of the 1D Bose–Hubbard model with high precision for fairly large system sizes. The main obstacle is related to the fact that, in principle, each lattice site can be occupied by infinitely many bosonic particles. Therefore, one has to introduce a cutoff n_b, the maximum number of bosons per site taken into account. The DMRG results are nonetheless unbiased and numerically exact, if the dependence on n_b can be proven to be negligible and a careful finite-size extrapolation to the thermodynamic limit ($L \to \infty$) has been performed.

Within the ground-state DMRG technique [21, 22] the energy functional

$$E(\psi) = \frac{\langle\psi|\hat{H}|\psi\rangle}{\langle\psi|\psi\rangle} \quad (60)$$

is minimized in a variational subspace in order to find the ground-state wave function $|\psi_0\rangle$ and energy $E_0 = E(\psi_0)$ whereby the DMRG energy error is proportional to the weight of the density-matrix eigenstates discarded in the renormalization process. Increasing the number m of density-matrix eigenstates kept, the discarded weight can be reduced systematically. Practically, the ground-state DMRG procedure mostly consists of two steps. During the infinite-system algorithm the system size is enlarged by two sites at each step and this operation has to be continued until the whole system reaches the desired system size L. Subsequently, a finite-system algorithm is used, where several sweeps through a lattice of fixed size L are performed. Thereby, the lattice is divided in two blocks with ℓ respectively $L-\ell$ sites where $1 \le \ell \le L-1$. This sweeping improves the quality of the results obtained in the infinite-system algorithm. We note that this procedure is perfectly suited to compute the von Neumann entanglement entropy on-the-fly in the finite-system algorithm. From this quantity, the KT transition point of the Bose–Hubbard model can be determined accurately.

The DMRG procedure can also be used to minimize the following functional [58, 59]:

$$\begin{aligned} W_{A,\eta}(\omega,\psi) = \langle\psi|(E_0+\omega-\hat{H})^2 + \eta^2|\psi\rangle \\ + \eta\langle A|\psi\rangle + \eta\langle\psi|A\rangle \ . \end{aligned} \quad (61)$$

Here, $\hat{H}$ is the (time-independent) Hamilton operator and $\hat{A}$ denotes the quantum operator of the physical quantity to be analyzed; $\hat{A}^\dagger$ is its Hermitian conjugate and $|A\rangle = \hat{A}|\psi_0\rangle$. Once this minimization has been carried out, the dynamical correlation function

$$G_{\hat{A}}(\omega+\mathrm{i}\eta) = -\frac{1}{\pi}\langle\psi_0|\hat{A}^\dagger \frac{1}{E_0+\omega+\mathrm{i}\eta-\hat{H}}\hat{A}|\psi_0\rangle, \quad (62)$$

can be evaluated. Here, the small real number η shifts the poles of the correlation function in the complex plane, i.e., η leads to a Lorentzian broadening of the peaks of the corresponding spectral function given in Lehmann representation as

$$\begin{aligned} I_{\hat{A}}(\omega+\mathrm{i}\eta) &= \mathrm{Im} G_{\hat{A}}(\omega+\mathrm{i}\eta) \\ &= \frac{1}{\pi}\sum_n |\langle\psi_n|\hat{A}|\psi_0\rangle|^2 \frac{\eta}{(E_n-E_0-\omega)^2+\eta^2} \ . \end{aligned} \quad (63)$$

Within this so-called dynamical DMRG (DDMRG) technique, the sweeps in the finite-system algorithm are repeated until both functionals, $E(\psi)$ and $W_{A,\eta}(\omega,\psi)$, take their minimal values.

Investigating the Bose–Hubbard model by DMRG, we keep up to $n_b = 5$ bosonic particles per site. Furthermore, we use $m = 2000$ density-matrix eigenstates in the DMRG runs for the ground-state expectation values. Then, the discarded weight is typically smaller than 10^{-10}. In the DDMRG calculations we keep $m = 500$ states to determine the ground state during the first five DMRG sweeps, and afterwards use $m = 300$ states for the calculation of the dynamical properties.

V. RESULTS AND DISCUSSION

A. von Neumann entanglement entropy

Previously, the KT transition point between the superfluid and insulating phases has been determined from the Luttinger parameter K_b [60, 61], which can be extracted from the density-density correlation function by DMRG, yielding $t_c = 0.305 \pm 0.001$ ($t_c = 0.180 \pm 0.001$) for $\rho = 1$ ($\rho = 2$) [20]. Although $K_b(t < t_c)$ is not defined in the MI, $K_b(L)$ is finite and continuous over the KT transition because the Mott gap is exponentially small. Therefore, it can be used within a DMRG finite-size extrapolation procedure.

The quantum phase transition should become manifest in the system's entanglement properties as well [62, 63]. An important measure to quantify the entanglement of two subsets of an interacting quantum system is the von Neumann entanglement entropy, which shows a logarithmic scaling for critical systems [64]. To determine the critical point between a Tomonaga–Luttinger liquid and gapped (or ordered) phases for more subtle situations, e.g. for frustrated spin models, spinless fermion models with nearest-neighbor interaction or fermion-boson transport models, the use of the entanglement entropy difference has been demonstrated to be advantageous [65–67].

For a block of length ℓ in a periodic system of the system size L, the von Neumann entropy, $S_L(\ell)$, is given by $S_L(\ell) = -\mathrm{Tr}_\ell(\rho_\ell \ln \rho_\ell)$, with the reduced density matrix $\rho_\ell = \mathrm{Tr}_{L-\ell}(\rho)$. One finds for PBC [68],

$$S_L(\ell) = \frac{c}{3} \ln\left[\frac{L}{\pi} \sin\left(\frac{\pi \ell}{L}\right)\right] + s_1 \,, \qquad (64)$$

where c is the central charge. When one evaluates the entropy difference $S_L(L/2) - S_{L/2}(L/4)$ using DMRG with open boundary conditions (OBC) [69], it includes the effect of the non-universal constant s_1. Therefore, the values for t_c cannot be extrapolated systematically. Here, we follow the alternative scheme proposed by Nishimoto [65]. We subtract $S_L(L/2)$ from $S_L(L/2-1)$ to obtain

$$c^*(L) \equiv \frac{3\,[S_L(L/2-1) - S_L(L/2)]}{\ln\,[\cos(\pi/L)]} \,. \qquad (65)$$

As $L \to \infty$, in the SF regime, the quantity $c^*(L)$ scales to the central charge $c = 1$ [68, 70].

Fig. 2 displays $c^*(L)$ for the 1D Bose–Hubbard model. Advantageously, we can use periodic boundary conditions for the calculation of this quantity. As shown in the insets, the position of the maximum in c^* can be reliably extrapolated to the thermodynamic limit. In this way we get the cone point of the Mott lobes $t_c = 0.305(3)$ for $\rho = 1$ and $t_c = 0.179(7)$ for $\rho = 2$ (in units of U), in excellent agreement with the previous estimates from the OBC finite-size scaling of K_b [20].

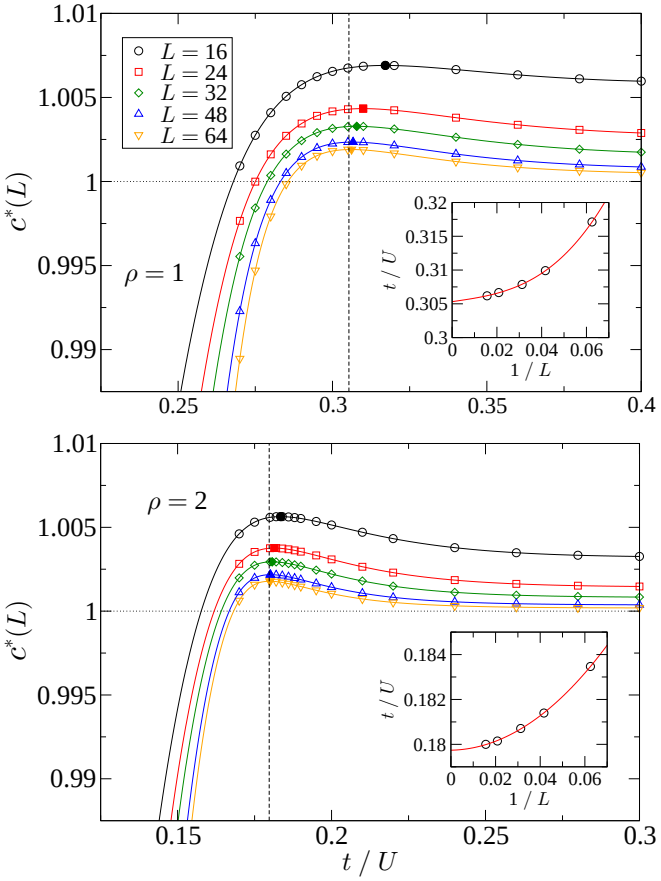

FIG. 2. (Color online) Entanglement entropy difference, c^* from Eq. (65), for the 1D Bose–Hubbard model with $\rho = 1$ (upper panel) and $\rho = 2$ (lower panel). Data obtained by DMRG for lattices up to $L = 64$ with PBC. The closed symbols indicate the maximum value for each system size. An extrapolation of the t/U values at these maxima to the thermodynamic limit provides the Kosterlitz–Thouless transition point, see insets; here, the lines correspond to a polynomial fit. The vertical dashed lines in the main panels mark the Kosterlitz–Thouless transition point.

B. Ground-state properties

1. Ground-state energy

The ground-state energy E_0 of the 1D Bose–Hubbard model has been determined analytically in the weak- and strong-coupling cases. For weak interactions, the Bogoliubov result was given in Eq. (6), with the small-U expansion given by Eq. (7). For strong interactions, an expansion up to 14th order in $x = t/U$ was obtained by Damski and Zakrzewski [30]:

$$\frac{E_0^{[14]}}{4UL} = -x^2 + x^4 + \frac{68}{9}x^6 - \frac{1267}{81}x^8 + \frac{44171}{1458}x^{10} - \frac{4902596}{6561}x^{12} - \frac{8020902135607}{2645395200}x^{14} + \mathcal{O}(x^{16}) \,. \tag{66}$$

Fig. 3 compares these perturbative results with our VCA and DMRG data. The VCA reproduces the DMRG results almost perfectly for all interaction strengths $t/U \leq 0.5$. The strong-coupling series expansion is also in accordance with the numerical exact data, surprisingly even beyond the KT transition point, i.e., for $t/U \lesssim 0.4$. Note that in Ref. [30] the ground-state energy (67) was compared with numerical data obtained for a system with $L = 40$ sites only. Hence, in their figure, the deviation starts at about $t \approx 0.2U$. Clearly, the quality of the strong-coupling approximation improves as higher-order corrections are taken into account, cf. the 4th-, 10th-, and 14th-order results. Fig. 3 also shows the range of validity of the corresponding weak-coupling approaches. Surprisingly, the Bogoliubov result is applicable up to the Mott transition point.

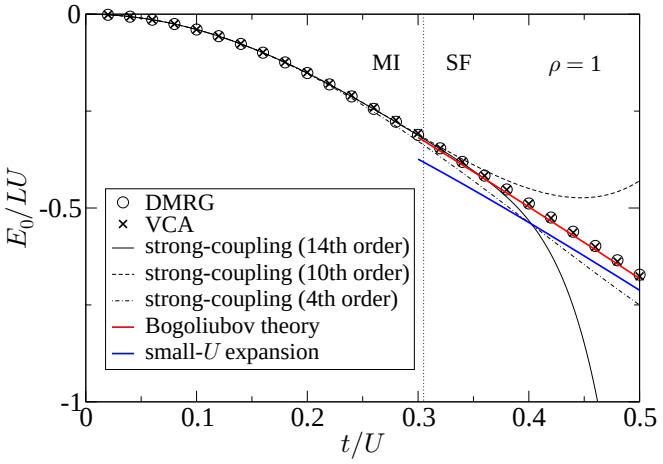

FIG. 3. (Color online) Ground-state energy, $E_0/(LU)$, as a function of interaction strength t/U for $\rho = 1$. Weak-coupling and strong-coupling results are compared with the $L \to \infty$ extrapolated DMRG data obtained from chains up to $L = 128$ with OBC. For the VCA calculations (crosses) a cluster with $L_c = 12$ ($L_c = 4$) sites is used in the MI (SF) phase.

2. Boson correlation function

In order to characterize the correlations in the ground-state of the interacting Bose gas described by the Bose–Hubbard model, it is instructive to look at the distance dependence of the expectation values $\langle \hat{b}_j^\dagger \hat{b}_\ell \rangle$, which, with appropriate normalization, constitute the matrix elements of the one-particle density matrix [3].

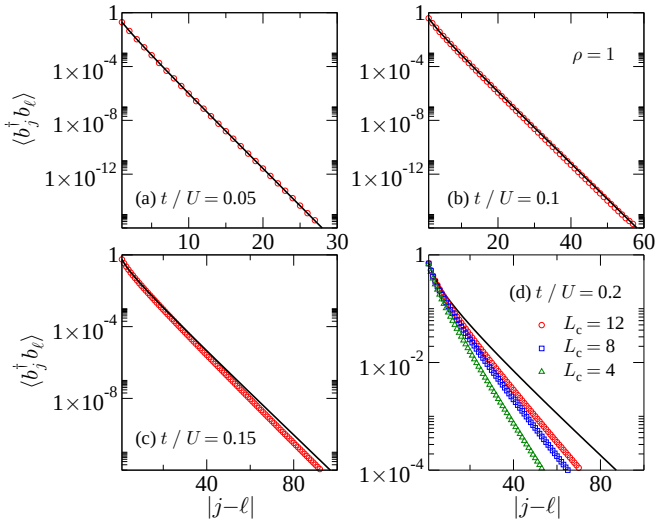

FIG. 4. (Color online) Decay of bosonic correlations in the 1D Bose–Hubbard model within the first Mott lobe ($\rho = 1$) for decreasing interaction strengths $x = 0.05$ (a), 0.1 (b), 0.15 (c), and 0.2 (d). DMRG results are obtained for a chain with $L = 128$ sites and OBC. To minimize the boundary effects we place j and ℓ symmetrically around the center of the system. The VCA data were calculated using clusters with $L_c = 4$ (green triangles), 8 (blue squares), and 12 (red circles).

In the gapless SF state, the boson single-particle correlation function

$$\langle \hat{b}_j^\dagger \hat{b}_\ell \rangle \sim |j - \ell|^{-K_b/2} \tag{67}$$

shows a power-law decay with an exponent determined by the Tomonaga–Luttinger parameter K_b [18].

In the insulating (gapped) MI, the bosonic correlations decay exponentially (at large distances), which is demonstrated by the semi-logarithmic representation in Fig. 4. At very strong couplings, the excitation gap is large and therefore can be obtained very accurately within VCA. As x becomes larger, i.e., U becoming smaller at fixed t, the correlations are significant over many lattice sites. In this regime, we find noticeable deviations of the VCA results if L_c is too small, see panel (d).

3. Momentum distribution function

The Fourier-transformed single-particle density matrix gives the momentum distribution function

$$n(k) = \frac{1}{L} \sum_{j,\ell=1}^{L} e^{\mathrm{i}k(j-\ell)} \langle \hat{b}_j^\dagger \hat{b}_\ell \rangle \ . \tag{68}$$

To third order in $x = t/U$, strong-coupling theory predicts for the first Mott lobe [10, 30]:

$$n^{[3]}(k) = 1 + (8x - 16x^3)\cos(k) + 36x^2 \cos(2k) + 176x^3 \cos(3k) \ . \tag{69}$$

In Fig. 5 we compare the strong-coupling expansion (69) with the DMRG and VCA numerics.

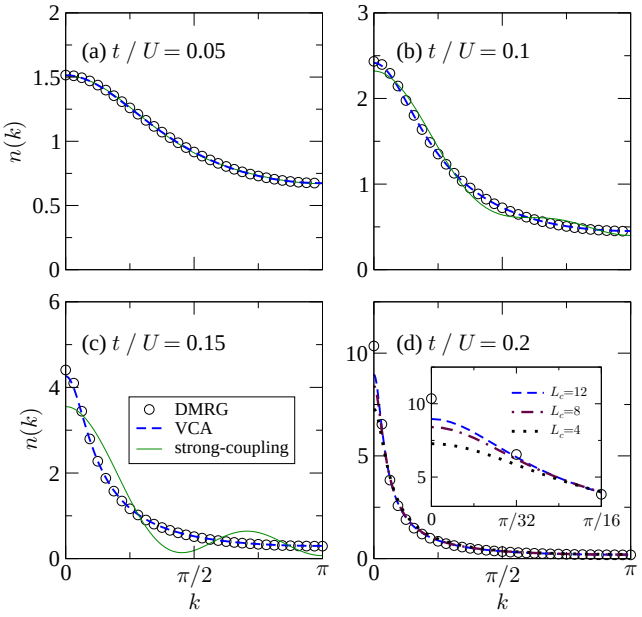

FIG. 5. (Color online) Momentum distribution function $n(k)$ within the first Mott lobe from DMRG with $L = 64$ and PBC (symbols), VCA (dashed lines), and third-order strong-coupling expansion (69) (solid lines). The inset in panel (d) shows the dependence of the VCA results on the cluster size L_c for $k \gtrsim 0$ in comparison with the DMRG data.

While for $t/U = 0.05$, where the momentum distribution is rather flat indicating weak site-to-site correlations, all methods essentially agree [see panel (a)], small deviations between analytical and numerical approaches appear for $t/U \gtrsim 0.1$ [panel (b)]. The oscillations emerging for $x \sim 0.15$ in the third-order strong-coupling theory are clearly an artifact. The VCA reproduces the density distribution $n(k)$ very well. However, it fails quantitatively for $k \to 0$ and $x = 0.2$ if the cluster used is not large enough, see the inset in panel (d).

When we approach the MI-SF KT transition point by raising x, $n(k = 0)$ will rapidly increase with system size. In 1D, of course, $n(k = 0)$ will not attain a macroscopic value in the thermodynamic limit because no true condensate develops [25]. Instead, we have from Eq. (67)

$$n(|k| \to 0) \sim |k|^{-\nu} \ , \ \nu = 1 - K_b/2 < 1 \ . \tag{70}$$

Thus far, it is difficult to reproduce this algebraic divergence in the SF phase; see, however, Ref. [71], where ν was determined by DMRG.

C. Dynamical quantities

1. Photoemission spectra and density of states

The single-particle excitations associated with the injection and emission of a boson with wave vector k and frequency ω, are described by the spectral functions $A^+(k,\omega)$ and $A^-(k,\omega)$, see Eqs. (27) and (28), respectively. These quantities can be evaluated by VCA [36] and DDMRG [58, 59]. For the Bose–Hubbard model the following sum-rules hold [cf. Eqs. (36), (37)]:

$$\int_{-\infty}^{\infty} \mathrm{d}\omega [A^+(k,\omega) - A^-(k,\omega)] = 1 \ , \tag{71}$$

$$\int_{-\infty}^{\infty} \mathrm{d}\omega A^-(k,\omega) = n(k) \ . \tag{72}$$

Summing over momenta k, the density of states $N(\omega)$ follows as

$$N(\omega) = A^+(\omega) - A^-(\omega) \ , \tag{73}$$

where $A^\pm(\omega) = \sum_k A^\pm(k,\omega)/L$. Within the DDMRG framework, however, it is much more appropriate to calculate $N(\omega)$ directly, instead of performing the k-summation of $A^\pm(k,\omega)$.

First, we discuss the spectral function, $A(k,\omega) = A^+(k,\omega) + A^-(k,\omega)$, and the density of states, $N(\omega)$, in the MI regime. The DDMRG spectra for fixed k consist of two Lorentzians of width $\eta = 0.04U$, which is the broadening introduced in the DDMRG procedure, cf. Sect. IV.

Fig. 6 shows the quasiparticle dispersions (squares) extracted from Lorentz fits to the maxima in $A^\pm(k,\omega)$. The quality of the fits suggests that the quasiparticle life-time is very large. Because of the large Mott gap separating single-particle and single-hole quasiparticle bands, the VCA can work with small cluster sizes and the quasiparticle spectra are in perfect agreement with the DDMRG data. The same holds for the strong-coupling results. In fact, for large interactions, each site is singly occupied in the ground state. As a consequence, a hole or doubly occupied site can move almost freely through the system. From this consideration, the leading-order expression for the quasiparticle dispersions results [20], see Eqs. (24) and (25). We note in passing that the simple mean-field approach by van Oosten et al. [72] fails to reproduce the quasiparticle dispersion already for $x = 0.1$, see Ref. [20].

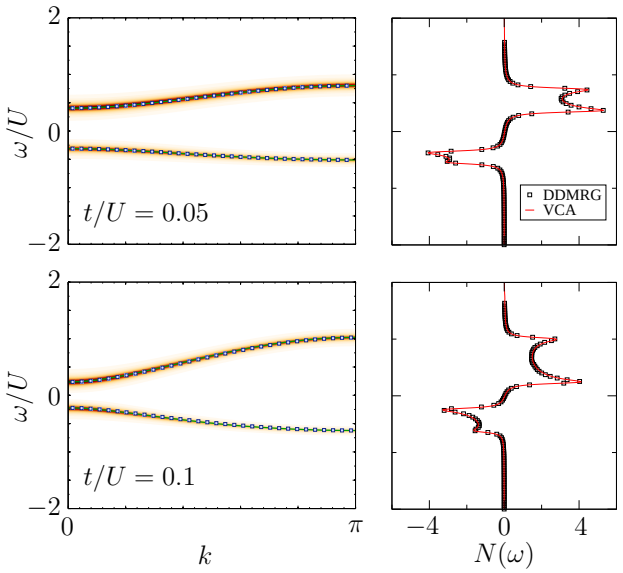

FIG. 6. (Color online) Single-particle spectral function $A(k,\omega)$ in the k-ω plane (left panels) and density of states $N(\omega)$ (right panels) for the 1D Bose–Hubbard model with $\rho = 1$ and $t/U = 0.05$ (upper panels), $t/U = 0.1$ (lower panels). We compare DDMRG data for a system with $L = 64$ and OBC (squares) with the results of VCA for $L_c = 12$ and $\eta = 0.03U$ (density plots) and strong-coupling expansions (24) and (25) (lines).

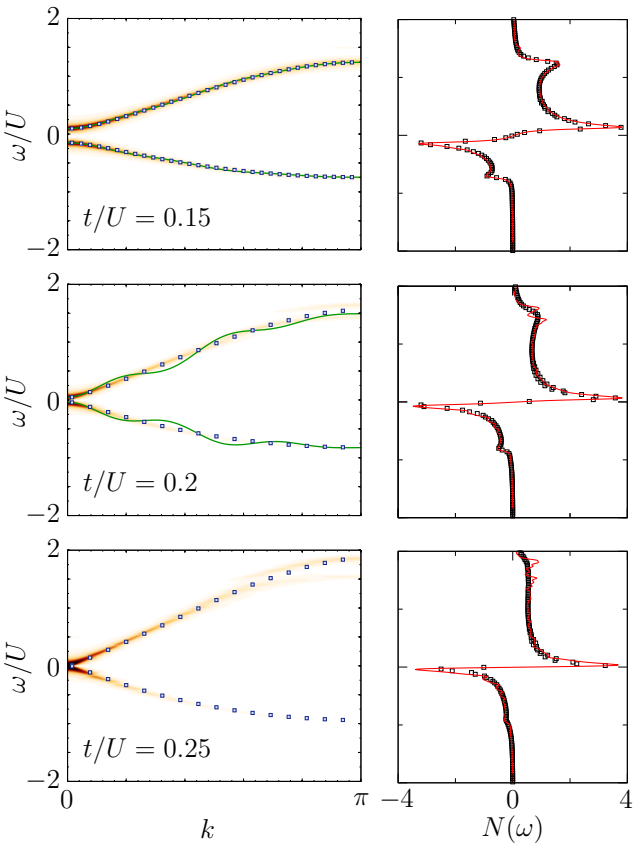

FIG. 7. (Color online) Spectral functions and density of states for intermediate couplings $t/U = 0.15$ (upper panels), $t/U = 0.2$ (middle panels) and $t/U = 0.25$ (lower panels). Notations are the same as in Fig. 6.

As the on-site interaction further weakens, the Mott gap gradually closes; the corresponding results are depicted in Fig. 7. Obviously, strong-coupling theory becomes imprecise at $x \approx 0.2$, and completely fails at $x \gtrsim 0.25$. There also VCA shows some artificial gap features near the Brillouin zone boundary, which do not show up in DDMRG.

In the superfluid phase, the elementary excitations concentrate around the region $(k = 0, \omega = 0)$, see Fig. 7 in Ref. [20], which indicates the formation of a "condensate". In accordance with Bogoliubov theory and field theory [26, 43], the low-energy, low-momentum excitations dominate the single-particle spectrum. As can be seen from Fig. 8, our spectral function indeed exhibits a phonon mode whose excitation energy –for a system in the thermodynamic limit– is linear in k and gapless at $k = 0$. Yet, for finite-size systems a gap is present whose magnitude is inversely proportional to the system size. Our DDMRG data demonstrate that the gap almost vanishes already for a OBC system with 64 sites. A similar behavior has been observed in QMC calculations which employ the directed-loop method [13].

Within the VCA, we find a larger gap as compared to DDMRG, due to the fact that we solve only four-site clusters exactly which are subsequently coupled perturbatively. In Ref. [36] we showed that the gap at $k = 0$ decreases with increasing cluster size, suggesting the correct behavior in the infinitely large cluster limit. Along the linear Goldstone modes, the spectral weight obtained by means of VCA exhibits fringes and a series of minigaps. This behavior is most likely a result of the cluster decomposition and subsequent periodization of the Green's function [35]. However, it should be emphasized that the slopes of the phonon mode obtained by the two methods agree very well.

A universal feature of systems with broken $U(1)$ symmetry is that, in addition to a gapless Goldstone mode, a gapped amplitude mode should be present. Whereas the Goldstone modes correspond to phase fluctuations, the amplitude modes arise from fluctuations in the magnitude of the order parameter. This behavior can be sketched by a Mexican hat potential for the order parameter [73]. It has been argued in Ref. [73] that the amplitude modes are sharp excitations in the quasiparticle sense only for dimensions $d \geq 3$ for which they were detected experimentally [74].

For $d < 3$ the decay of the amplitude modes into Goldstone modes is very efficient and, thus, the weight observed in the susceptibilities can be redistributed over a large frequency range. This renders an observation of the amplitude modes difficult. In 2D it was demon-

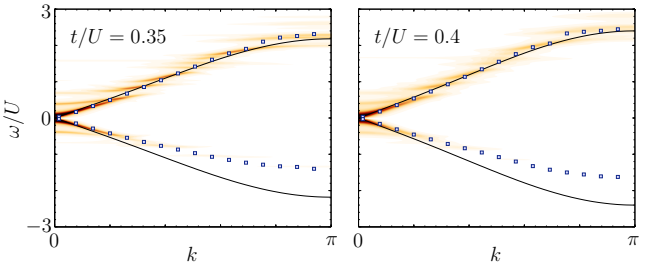

FIG. 8. (Color online) Spectral functions in the superfluid phase of the 1D Bose–Hubbard model with $t/U = 0.35$ (left panel), $t/U = 0.4$ (right panel). Compared are DDMRG dispersions with VCA density plots for $L_c = 4$ and the dispersion of the condensate excitations $E(k)$ from Bogoliubov theory (black lines, other symbols are the same as in Fig. 6); see Eq. (3) with (2).

strated theoretically that the coupling to the amplitude modes can be improved by evaluating susceptibilities for the kinetic energies [75] or for operators that resemble the rotationally invariant structure of the Mexican hat potential [76]. This should result in clearer signals for the amplitude modes in the respective response functions. Indeed, in setups with ultracold atoms, recent lattice modulation experiments, which couple directly to the amplitude modes, provide evidence for their existence in 2D [77].

In 1D where no true condensate exists, the spectral smearing of the amplitude modes is believed to be even more pronounced. Our numerical DMRG and VCA results for the spectral function and the dynamical structure factor, which both couple to the gapless Goldstone mode and the amplitude mode, give no indication for the latter. Therefore, we do not expect that an amplitude mode will be observed in Bragg spectroscopy experiments for bosons in one dimension. It is quite remarkable that VCA reproduces the overall character of the single-particle spectrum consisting of Goldstone modes only, despite of the fact that, technically, a spurious condensate has to be introduced to treat the superfluid phase, see Sec. III for a detailed discussion.

2. *Dynamic density-density correlations*

We now turn to the dynamical density-density response function. We carry out large-scale DDMRG calculations of the dynamic structure factor, $S(q,\omega)$, and compare the results with the predictions of strong-coupling theory (40) where appropriate. In strong coupling, we show results in fourth-order approximation. The agreement with the DDMRG data for $x = 0.15$ improves noticeably when we calculate expectation values with $|q\rangle \approx \sum_{n=1}^{5} x^n |q^{[n]}\rangle$ from (38), i.e., we keep the states to fifth order in x.

Since DDMRG provides $S(q,\omega)$ with a finite broadening η, it turns out to be useful to convolve the strong-coupling result with the Lorentz distribution [78],

$$S_\eta(q,\omega) = \int_{-\infty}^{\infty} \mathrm{d}\omega' S(q,\omega') \frac{\eta}{\pi\left[(\omega-\omega')^2+\eta^2\right]} \,. \quad (74)$$

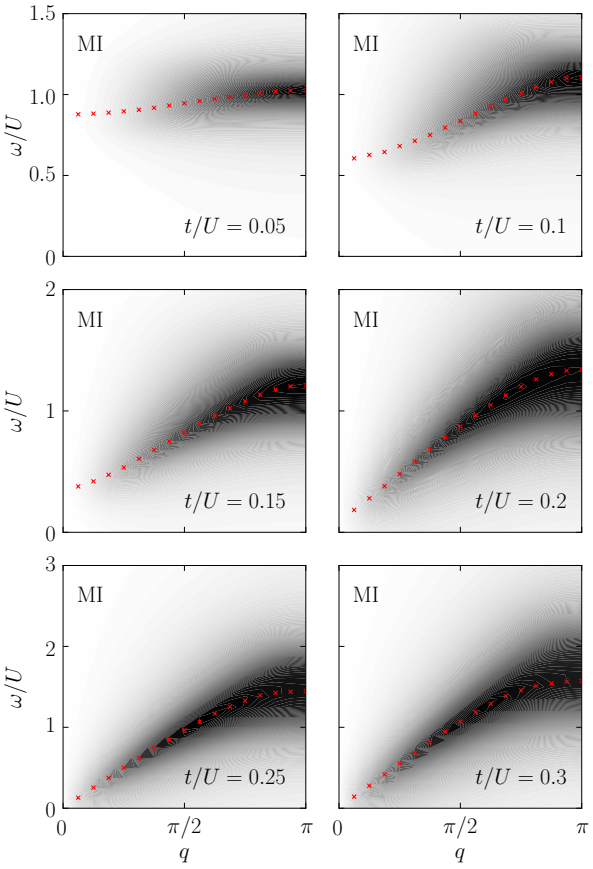

FIG. 9. (Color online) Intensity of the dynamical structure factor $S(q,\omega)$ in the MI phase of the 1D Bose–Hubbard model for different t/U where $\rho = 1$. DDMRG data were obtained for an $L = 32$ site system with PBC, using $\eta = 0.5t$. Red crosses mark the positions of the maximum in each $q = 2\pi m_q/L$-sector.

Mott phase. Fig. 9 illustrates the change of the intensity distribution of $S(q,\omega)$ in the q-ω plane as $x = t/U$ increases in the MI regime. For small x, deep in the MI, the spectral weight is concentrated around $\omega \sim U$ in the region $q > \pi/2$ (cf. the upper left panel). This meets the predictions of the strong-coupling theory [53]. In this regime the structure factor is dominated by the primary band.

When x increases, the maximum of $S(q,\omega)$ acquires an appreciable dispersion; simultaneously the overall intensity of the density-density response strengthens, see the middle panels of Fig. 9 and also Fig. 10. As the system approaches the MI-SF transition point, the excitation gap closes. Concomitantly, we find a significant redistribution of the spectral weight to smaller q values,

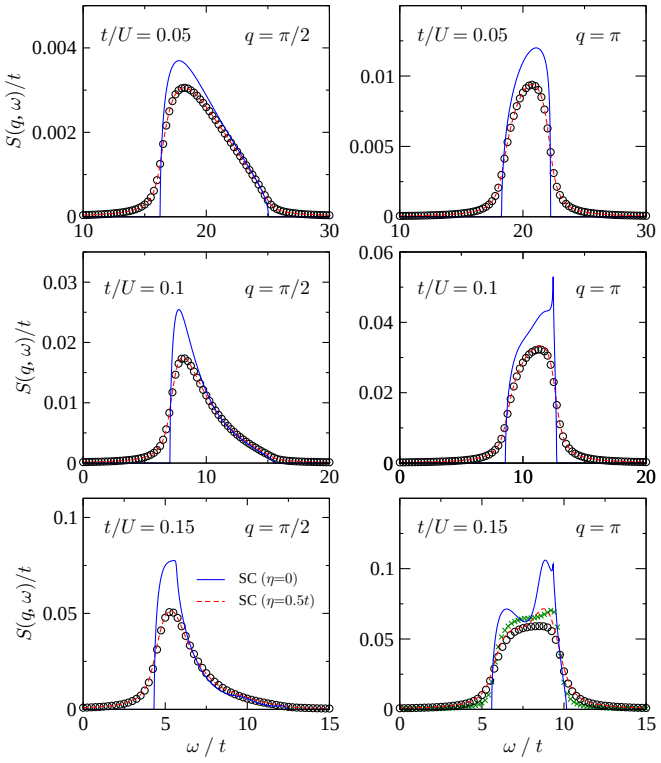

FIG. 10. (Color online) Frequency-scans of the dynamical structure factor in the MI state at fixed momenta $q = \pi/2$ (left panels), $q = \pi$ (right panels). DDMRG data (circles) were obtained for $L = 64$, PBC, and $\eta = 0.5t$; at $t/U = 0.15$ ($q = \pi$) also for $L = 128$, PBC, and $\eta = 0.2t$ (green crosses). Blue solid (red dashed) lines give the corresponding results of the strong-coupling theory with $\eta = 0$ ($\eta = 0.5t$). Please note the different scales of the ordinates.

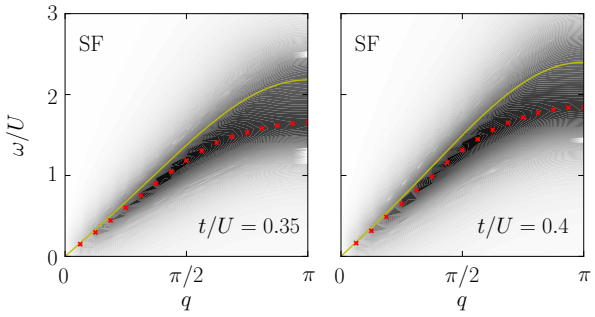

FIG. 11. (Color online) Intensity of the dynamical structure factor $S(q, \omega)$ in the superfluid phase of the Bose–Hubbard model with $\rho = 1$. Again we use $L = 32$, PBC, and $\eta = 0.5t$. The yellow line gives the Bogoliubov result (3).

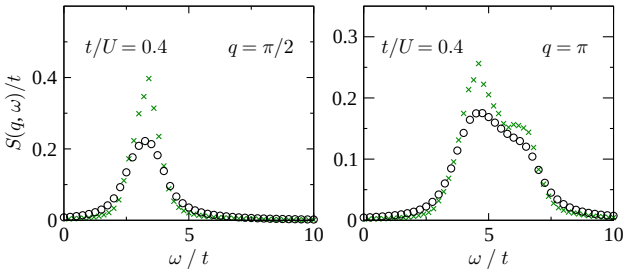

FIG. 12. (Color online) Frequency dependence of the dynamical structure factor $S(q, \omega)$ at $q = \pi/2$ and $q = \pi$. Only DDMRG data are shown. Circles (crosses) mark the results for $L = 64$, PBC, and $\eta = 0.5t$ ($L = 128$, PBC, and $\eta = 0.2t$).

see the lower panels of Fig. 9.

In Fig. 10 we show constant-moment scans of $S(q, \omega)$ at $q = \pi/2$ and $q = \pi$. For $x = 0.05$ and $x = 0.10$, the agreement between the broadened strong-coupling results and the DDMRG data for $S(q, \omega)$ is excellent. As x becomes larger than $x \approx 0.10$, the strong-coupling theory yields a double-peak structure in $S(\pi, \omega)$. When we increase the lattice size and reduce η, this feature also appears in our DDMRG data for $t/U = 0.15$. Therefore, this feature is not an artifact of the strong-coupling approach even though the strong-coupling expansion overestimates the double-peak structure for $x = 0.15$. The strong-coupling expansion solves an effective single-particle problem in a (finite-range, attractive) potential. Such a potential gives rise to a non-trivial spectrum (resonances and possibly bound states). The energy levels of the effective single-particle problem lead to non-trivial spectral signatures in the dynamical structure factor.

Superfluid phase. Figs. 11 and 12 present the corresponding results for the dynamical structure factor in the SF phase. At small momenta, Bogoliubov theory gives the correct slope of the dispersion which we derive from the maximum of the DDMRG data for $S(q, \omega)$. Note that the dispersion $E(q)$ in (3) is identical to the predictions from field theory [18]. Bogoliubov's dispersion overestimates the DDMRG maxima for larger momenta and higher energies, as observed experimentally for a 3D setup [41]. As compared to the MI phase, the density-density response has higher intensity in the SF state. Interestingly, we also find a shoulder in $S(\pi, \omega)$, which may form a double peak as $L \to \infty$, $\eta \to 0$, see the right-hand panel of Fig. 12. This high-energy double peak in the SF phase resembles the structure seen in the MI phase. In our opinion, this rules out an interpretation of the second peak as signature of a massive Higgs mode [28].

VI. SUMMARY

The aim of this paper was twofold: (i) to provide extensive numerical (D)DMRG data for static and dynamical quantities of the one-dimensional Bose–Hubbard model at integer filling, mostly for $\rho = N/L = 1$; (ii) to compare the (D)DMRG results with the analytical strong coupling perturbation theory and the numerically inexpensive VCA and thereby explore their merits and limi-

tations in the most demanding case of one dimension.

We used the DMRG to calculate the central charge from which we confirmed the critical values for the superfluid to Mott transition for integer fillings $\rho = 1$ and $\rho = 2$.

The ground-state energy from DMRG compares favorably with results from VCA and from perturbation theory. For static correlation functions such as the single-particle density matrix and the momentum distribution, the comparison between DMRG data and strong-coupling perturbation theory (VCA) shows that the latter are reliable for $x = t/U \lesssim 0.15$ ($x \lesssim 0.25$), for doable implementations.

We calculated dynamical quantities such as the single-particle spectral function and the dynamical structure factor. In the superfluid phase, the response at low energies is dominated by the quasi-condensate, in agreement with predictions from field theory and Bogoliubov theory. The latter provides the correct result for the phonon mode despite the fact that it is based on the incorrect assumption of a true condensate. For finite interactions and at higher energies, the dynamical structure factor is broad and reflects the physics of the Mott insulator. The overall character of the single-particle spectrum and the sound velocity of the phonon modes are reproduced by VCA for larger values of x.

The strong-coupling results for the dynamical structure factor helped us to interpret our numerical DDMRG data because the latter are spectrally broadened for finite system sizes. The two-particle correlation function in the Mott phase reflects the (scattering) states of a doubly occupied site and a hole with a hard-core repulsion and a (weak) longer-ranged attraction giving rise to a double-peak structure in the dynamical structure factor near the boundary of the Brillouin zone.

Our numerical work can be compared with experiments only after the parabolic confinement potentials will have been taken into account. Important as it is to confine the atoms to the optical lattice, the confinement potential often is so strong that the density profile contains several Mott regions with different integer fillings and transition regions between them. In this case, the structure factor at low energies describes the dynamical response of the 'wedding-cake' density profile [79, 80].

There are two other directions to extend our work. The Mott gap in the Bose–Hubbard model resembles a band gap. Therefore, it is interesting to see how bound states ('excitons') form in this gap in the presence of a nearest-neighbor attraction. A second route to extend our work is the inclusion of a disorder potential [26, 81, 82] so that the smearing and closing of the Mott gap as a function of the disorder can be studied. Work in this direction is in progress.

ACKNOWLEDGMENTS

The authors thank I. Danshita, G. Hager, E. Jeckelmann, H. Monien, S. Nishimoto, and W. Zwerger for valuable discussions. Financial support by the Deutsche Forschungsgemeinschaft through the SFB 652 and by the Austrian Science Fund (FWF) P24081-N16 are gratefully acknowledged.

[1] M. Greiner, O. Mandel, T. Esslinger, T. W. Hänsch, and I. Bloch, Nature **415**, 39 (2002).
[2] M. Greiner, O. Mandel, T. W. Hänsch, and I. Bloch, Nature **419**, 51 (2002).
[3] C. Kollath, U. Schollwöck, J. von Delft, and W. Zwerger, Phys. Rev. A **69**, R031601 (2004).
[4] I. Bloch, J. Dalibard, and W. Zwerger, Rev. Mod. Phys. **80**, 885 (2008).
[5] G. Grynberg, P. Horak, and C. Mennerat-Robilliard, Europhys. Lett. **49**, 424 (2000).
[6] P. Lugan, D. Clément, P. Bouyer, A. Aspect, M. Lewenstein, and L. Sanchez-Palencia, Phys. Rev. Lett. **98**, 170403 (2007).
[7] D. Jaksch, C. Bruder, J. I. Cirac, C. W. Gardiner, and P. Zoller, Phys. Rev. Lett. **81**, 3108 (1998).
[8] M. P. A. Fisher, P. B. Weichman, G. Grinstein, and D. S. Fisher, Phys. Rev. B **40**, 546 (1989).
[9] N. Teichmann, D. Hinrichs, M. Holthaus, and A. Eckardt, Phys. Rev. B **79**, 224515 (2009).
[10] J. K. Freericks, H. R. Krishnamurthy, Y. Kato, N. Kawashima, and N. Trivedi, Phys. Rev. A **79**, 053631 (2009).
[11] W. Krauth and N. Trivedi, Europhys. Lett. **14**, 627 (1991).
[12] G. G. Batrouni, V. Rousseau, R. T. Scalettar, M. Rigol, A. Muramatsu, P. J. H. Denteneer, and M. Troyer, Phys. Rev. Lett. **89**, 117203 (2002).
[13] P. Pippan, H.-G. Evertz, and M. Hohenadler, Phys. Rev. A **80**, 033612 (2009).
[14] B. Capogrosso-Sansone, N. V. Prokov'ev, and B. V. Svistunov, Phys. Rev. B **75**, 134302 (2007).
[15] Y. Kato, Q. Zhou, N. Kawashima, and N. Trivendi, Nat. Phys. **4**, 617 (2008).
[16] T. Stöferle, H. Moritz, C. Schori, M. Köhl, and T. Esslinger, Phys. Rev. Lett. **92**, 130403 (2004).
[17] G. G. Batrouni, R. T. Scalettar, and G. T. Zimanyi, Phys. Rev. Lett. **65**, 1765 (1990).
[18] T. Giamarchi, *Quantum Physics in One Dimension* (Oxford University Press, Oxford, 2004).
[19] M. J. Mark, E. Haller, K. Lauber, J. G. Danzl, A. Janisch, H. P. Büchler, A. J. Daley, and H. Nägerl, arXiv:1201.1008.
[20] S. Ejima, H. Fehske, and F. Gebhard, Europhys. Lett. **93**, 30002 (2011).
[21] S. R. White, Phys. Rev. Lett. **69**, 2863 (1992).
[22] S. R. White, Phys. Rev. B **48**, 10345 (1993).
[23] T. D. Kühner and H. Monien, Phys. Rev. B **58**, R14741 (1998).
[24] T. D. Kühner, S. R. White, and H. Monien, Phys. Rev. B **61**, 12474 (2000).
[25] C. Mora and Y. Castin, Phys. Rev. A **67**, 053615 (2003).

[26] M. A. Cazalilla, R. Citro, T. Giamarchi, E. Orignac, and M. Rigol, Rev. Mod. Phys. **83**, 205301 (2011).
[27] T. Giamarchi, Phys. Rev. B **46**, 342 (1992).
[28] S. D. Huber, E. Altman, H. P. Büchler, and G. Blatter, Phys. Rev. B **75**, 085106 (2007).
[29] J. K. Freericks and H. Monien, Phys. Rev. B **53**, 2691 (1996).
[30] B. Damski and J. Zakrzewski, Phys. Rev. A **74**, 043609 (2006).
[31] N. Elstner and H. Monien, arXiv:cond-mat/9905367.
[32] N. Elstner and H. Monien, Phys. Rev. B **59**, 12184 (1999).
[33] C. Heil and W. von der Linden, arXiv:1105.2418 [J. Phys.: Condens. Matter (to be published)].
[34] W. Koller and N. Dupuis, J. Phys.: Condens. Matt. **18**, 9525 (2006).
[35] M. Knap, E. Arrigoni, and W. von der Linden, Phys. Rev. B **81**, 024301 (2010).
[36] M. Knap, E. Arrigoni, and W. von der Linden, Phys. Rev. B **83**, 134507 (2011).
[37] E. Arrigoni, M. Knap, and W. von der Linden, Phys. Rev. B **84**, 014535 (2011).
[38] M. Potthoff, Eur. Phys. J. B **32**, 429 (2003).
[39] D. Clément, N. Fabbri, L. Fallani, C. Fort, and M. Inguscio, Phys. Rev. Lett. **102**, 155301 (2009).
[40] N. Fabbri, D. Clément, L. Fallani, C. Fort, M. Modugno, K. M. R. van der Stam, and M. Inguscio, Phys. Rev. A **79**, 043623 (2009).
[41] P. T. Ernst, S. Götze, J. S. Krauser, K. Pyka, D.-S. Lühmann, D. Pfannkuche, and K. Sengstock, Nature Physics **6**, 56 (2009).
[42] X. Du, S. Wan, E. Yesilada, C. Ryu, D. J. Heinzen, Z. Liang, and B. Wu, New J. Phys. **12**, 083025 (2010).
[43] N. N. Bogoliubov, J. Phys. (USSR) **11**, 23 (1947).
[44] A. L. Fetter and J. D. Walecka, *Quantum theory of many-particle systems* (McGraw-Hill Publishing Company, Berlin, Heidelberg, 1971).
[45] Wolfram Research, Inc., *Mathematica*, Version 7.0 (Wolfram Research, Inc., Champaign, IL, USA, 2008).
[46] A. B. Harris and R. V. Lange, Phys. Rev. **157**, 295 (1967).
[47] P. G. J. van Dongen, Phys. Rev. B **49**, 7904 (1994).
[48] K. zu Münster, M.Sc. thesis, University of Marburg (2012).
[49] S. Nishimoto, F. Gebhard, and E. Jeckelmann, J. Phys.: Condens. Matt. **16**, 7063 (2004).
[50] M. Knap, E. Arrigoni, and W. von der Linden, Phys. Rev. B **81**, 235122 (2010).
[51] A. Iucci, M. A. Cazalilla, A. F. Ho, and T. Giamarchi, Phys. Rev. A **73**, 041608 (2006).
[52] A. Tokuno and T. Giamarchi, Phys. Rev. Lett. **106**, 205301 (2011).
[53] S. Ejima, H. Fehske, and F. Gebhard, arXiv:1110.4498 [J. Phys.: Conf. Series (to be published)].
[54] E. N. Economou, *Green's Functions in Quantum Physics* (Springer, Berlin, 1983).
[55] M. Potthoff, M. Aichhorn, and C. Dahnken, Phys. Rev. Lett. **91**, 206402 (2003).
[56] M. Potthoff, Eur. Phys. J. B **36**, 335 (2003).
[57] M. G. Zacher, R. Eder, E. Arrigoni, and W. Hanke, Phys. Rev. B **65**, 045109 (2002).
[58] E. Jeckelmann, Phys. Rev. B **66**, 045114 (2002).
[59] E. Jeckelmann and H. Fehske, Rivista del Nuovo Cimento **30**, 259 (2007).
[60] F. D. M. Haldane, Phys. Rev. Lett. **47**, 1840 (1981).
[61] C. Moseley, O. Fialko, and K. Ziegler, Ann. Phys. (Berlin) **17**, 561 (2008).
[62] L. Wang, K. S. D. Beach, and A. W. Sandvik, Phys. Rev. B **73**, 014431 (2006).
[63] S. Rachel, N. Laflorencie, H. F. Song, and K. Le Hur, Phys. Rev. Lett. **108**, 116401 (2012).
[64] M. A. Cazalilla, J. Phys. B. **37**, S1 (2004).
[65] S. Nishimoto, Phys. Rev. B **84**, 195108 (2011).
[66] S. Ejima, M. J. Bhaseen, M. Hohenadler, F. H. L. Essler, H. Fehske, and B. D. Simons, Phys. Rev. Lett. **106**, 015303 (2011).
[67] H. Fehske, S. Ejima, G. Wellein, and A. R. Bishop, arXiv:1110.4486 [J. Phys.: Conf. Series (to be published)].
[68] P. Calabrese and J. Cardy, J. Stat. Mech. P06002 (2004).
[69] A. M. Läuchli and C. Kollath, J. Stat. Mech. P05018 (2008).
[70] N. Laflorencie, E. S. Sørensen, M.-S. Chang, and I. Affleck, Phys. Rev. Lett. **96**, 100603 (2006).
[71] M. J. Bhaseen, S. Ejima, F. H. L. Essler, M. Hohenadler, H. Fehske, and B. D. Simons, Phys. Rev. A **85**, 033636 (2012).
[72] D. van Oosten, P. van der Straten, and H. T. C. Stoof, Phys. Rev. A **63**, 053601 (2001).
[73] S. Sachdev, *Quantum Phase Transitions* 2nd ed. (Cambridge University Press, Cambridge, 2011).
[74] U. Bissbort, S. Götze, Y. Li, J. Heinze, J. S. Krauser, M. Weinberg, C. Becker, K. Sengstock, and W. Hofstetter, Phys. Rev. Lett. **106**, 205303 (2011).
[75] L. Pollet and N. V. Prokof'ev, arXiv:1204.5190.
[76] D. Podolsky, A. Auerbach, and D. P. Arovas, Phys. Rev. B **84**, 174522 (2011).
[77] M. Endres, T. Fukuhara, D. Pekker, M. Cheneau, P. Schauß, C. Gross, E. Demler, S. Kuhr, and I. Bloch, arXiv:1204.5183.
[78] S. Nishimoto and E. Jeckelmann, J. Phys.: Condens. Matt. **16**, 613 (2004).
[79] G. G. Batrouni, F. F. Assaad, R. T. Scalettar, and P. J. H. Denteneer, Phys. Rev. A **72**, 031601 (2005).
[80] G. Pupillo, A. M. Rey, and G. G. Batrouni, Phys. Rev. A **74**, 013601 (2006).
[81] S. Rapsch, U. Schollwöck, and W. Zwerger, Europhys. Lett. **46**, 559 (1999).
[82] M. Knap, E. Arrigoni, and W. von der Linden, Phys. Rev. A **82**, 053628 (2010).